nature communications

Article

https://doi.org/10.1038/s41467-025-58000-4

Coupling furfural oxidation for bias-free hydrogen production using crystalline silicon photoelectrodes

Received: 29 July 2024

Accepted: 10 March 2025

Published online: 19 March 2025

Check for updates

Myohwa Ko[1,6], Myounghyun Lee[1,6], Taehyeon Kim[1,6], Wonjoo Jin[1,6], Wonsik Jang[2,6], Seon Woo Hwang[1], Haneul Kim[1], Ja Hun Kwak[1], Seungho Cho[2,3] ✉, Kwanyong Seo[1,4] ✉ & Ji-Wook Jang[1,4,5] ✉

To commercialize the technology of photoelectrochemical hydrogen production, it is essential to surpass the US. Department of Energy target of 0.36 mmol h^{-1} cm^{-2} for 1-sun hydrogen production rate. In this study, we utilize crystalline silicon, which can exhibit the highest photocurrent density (43.37 mA cm^{-2}), as the photoelectrode material. However, achieving bias-free water splitting (>1.6 V) remains challenging due to the intrinsic low photovoltage of crystalline silicon (0.6 V). To address this limitation, we replace water oxidation with low-potential furfural oxidation, enabling not only bias-free hydrogen production but also dual hydrogen production at both the cathodic and anodic sides. This approach results in a record 1-sun hydrogen production rate of 1.40 mmol h^{-1} cm^{-2}, exceeding the Department of Energy target by more than fourfold.

The pressing need to develop alternative energy sources to replace fossil fuels has become increasingly urgent amid growing environmental concerns. In this context, photoelectrochemical (PEC) hydrogen (H_2) production emerges as one of the most promising technologies, capable of converting inexhaustible solar energy into storable and clean fuels[1–5]. Despite dedicated efforts over the past few decades toward the practical implementation of PEC H_2 production, current 1-sun H_2 production rates fall short of reaching practical levels, as defined by the US Department of Energy's (DOE) ultimate target of 0.36 mmol h^{-1} cm^{-2}. Notably, this DOE target is conservatively set, assuming a target price of $2.1/1 kg of H_2[6]. However, to commercialize this PEC H_2 production technology, the target H_2 price should compete with that of H_2 produced from fossil fuels ($0.5–1/kg), which currently constitutes over 90% of H_2 production[7]. Thus, achieving 1-sun H_2 production rate two to four times higher than the DOE target, corresponding to 40–80 mA cm^{-2} of photocurrent density, is imperative to practicalize the PEC H_2 production technology.

We selected crystalline silicon (c-Si) as the material for the photocathode because it exhibits the highest photocurrent density among all reported photoelectrodes, which potentially exhibit a theoretical photocurrent density of 43.37 mA cm^{-2}, attributed to its small band gap of 1.1 eV[8,9]. This indicates the potential for maximizing 1-sun H_2 production rate using c-Si. Moreover, its Earth abundance and mature production technologies also make it a promising candidate for photoelectrode material[10]. However, a significant challenge in employing c-Si as a photoelectrode is that the photovoltage of c-Si (~0.6 V) is not high enough to provide sufficient photovoltage required for conventional water splitting (>1.6 V)[11]. In particular, water oxidation accounts for a large portion of required photovoltage. Accordingly, most c-Si-based PEC studies have reported half-cell-based performances, which require an additional external bias for overall water splitting[12,13].

[1]School of Energy and Chemical Engineering, Ulsan National Institute of Science and Technology (UNIST), Ulsan, Republic of Korea. [2]Department of Materials Science and Engineering, Ulsan National Institute of Science and Technology (UNIST), Ulsan, Republic of Korea. [3]Graduate School of Semiconductor Materials and Devices Engineering, Center for Future Semiconductor Technology (FUST), Ulsan National Institute of Science and Technology (UNIST), Ulsan, Republic of Korea. [4]Graduate School of Carbon Neutrality, Ulsan National Institute of Science and Technology (UNIST), Ulsan, Republic of Korea. [5]Emergent Hydrogen Technology R&D Center, Ulsan National Institute of Science and Technology (UNIST), Ulsan, Republic of Korea. [6]These authors contributed equally: Myohwa Ko, Myounghyun Lee, Taehyeon Kim, Wonjoo Jin, Wonsik Jang. ✉e-mail: scho@unist.ac.kr; kseo@unist.ac.kr; jiwjang@unist.ac.kr

Hence, to achieve bias-free water splitting, c-Si photoelectrode has essentially been coupled with another wide bandgap photoelectrode (like TiO_2, $BiVO_4$, WO_3, etc), but this union restricts the overall operating photocurrent to a range of 1–5 mA cm^{-2}, primarily due to the relatively low photocurrent density of the wide bandgap photoelectrode[14–17]. Alternatively, various research groups have explored different approaches, such as employing c-Si tandem devices or modularization techniques. These methods involve creating multi-junction configurations with c-Si and another semiconductor or interconnecting individual c-Si unit solar cells in series. The objective of such strategies is to elevate the photovoltage of the photoelectrode, thereby enabling bias-free water splitting without relying on a secondary photoelectrode[18–21]. However, despite the advancements, the enhancements in photovoltage often come at the cost of a notable reduction in photocurrent density, typically in the range of 8–13 mA cm^{-2}. This trade-off lowers the maximum achievable photocurrent density of c-Si. Consequently, none of these approaches have fully harnessed the high photocurrent density potential offered by a single c-Si photoelectrode for bias-free H_2 production.

In our study, we replace water oxidation with low-potential aldehyde oxidation to reduce the required photovoltage for PEC H_2 production. Consequently, a single c-Si photoelectrode can generate H_2 without external bias or the need for a secondary photoelectrode. Additionally, this low-potential aldehyde oxidation process yields both H_2 and valuable carboxylic acid simultaneously[22], contrasting with the relatively less valuable O_2 produced through water oxidation. Thus, a single c-Si photoelectrode can drive dual H_2 production at both the anode and cathode, effectively utilizing its high photocurrent on both sides. Furthermore, we fabricated a highly efficient p-n junction-based c-Si photocathode using an interdigitated back contact (IBC) structure c-Si solar cell, which shows higher short-circuit current density (J_{SC}) and open-circuit voltage (V_{OC}) compared to conventional structures[23,24]. Moreover, we revealed that the cooling effect induced by the electrolyte helps mitigate temperature rise, allowing the c-Si photocathode to operate at its maximum photovoltage. As a result of these advancements, we demonstrate dual PEC H_2 production with a remarkable photocurrent density of 37.6 mA cm^{-2} and an H_2 Faradaic efficiency of 200% (equivalent to 75.2 mA cm^{-2} for both sides of H_2 production). This achievement translates to a high H_2 production rate of 1.40 mmol h^{-1} cm^{-2}, which surpasses the DOE target by approximately fourfold.

Results

Design of bias-free dual H_2 production system

Conventional water splitting, involving the oxygen evolution reaction (OER) and hydrogen evolution reaction (HER), is simple, and the produced O_2 is environmentally benign. However, OER demands a high thermodynamic potential (1.23 V vs. reversible hydrogen electrode (RHE)), and its substantial overpotential, attributed to sluggish reaction kinetics, further increases the required photovoltage of the PEC cell beyond 1.6 V[2,11]. Consequently, the photovoltage of a c-Si photocathode (~0.6 V) is insufficient for overall water splitting (Fig. 1a). Alternatively, OER can be supplanted by reactions that are thermodynamically more favorable and yield higher-value products than O_2. Recently, Wang et al. reported a low-potential aldehyde oxidation, showing that 5-hydroxymethyl furfural oxidation concurrently produces the corresponding carboxylic acid (5-hydroxymethyl-2-furancarboxylic acid) and H_2 on a metallic Cu surface at a low onset potential of 0.05 V vs. RHE[22]. This approach can significantly reduce the required photovoltage for PEC H_2 production. As depicted in Fig. 1a, linear sweep voltammetry (LSV) curves of low-potential aldehyde oxidation and HER on a c-Si photocathode can achieve identical current levels at the same potential, indicating the capability for bias-free operation, unlike conventional water splitting. Thus, we devised a PEC system for dual H_2 production by conducting water reduction on a PtC/Ni/c-Si photocathode and furfural oxidation on a Cu anode (Fig. 1b). Furfural, a biomass-derived platform molecule, boasts a global production exceeding 430 kt/year[25]. Furthermore, furoic acid, the oxidative carboxylic acid product, serves as a valuable feedstock in the pharmaceutical, flavor, and polymer industries[26]. Industrial furoic acid is typically produced via the Cannizzaro reaction, where furfural in a concentrated alkaline solution yields furoic acid along with a stoichiometric amount of furfuryl alcohol as a byproduct. By contrast, the electrochemical furfural oxidation reaction not only produces furoic acid but also generates H_2 with minimal byproduct formation. Furthermore, the production of furoic acid ($6.23 kg^{-1}) and H_2 ($0.5–1 kg^{-1}) at the anode is economically attractive compared with other less valuable oxidation products (e.g., O_2: $0.02–0.04 kg^{-1}, H_2O_2: $0.57 kg^{-1}, acetic acid: $0.68–0.92 kg^{-1}, acetone: $0.9–1.28 kg^{-1}, and formic acid: $0.97–1.08 kg^{-1})[27]. The simultaneous production of furoic acid and H_2 during the low-potential furfural oxidation on Cu enables H_2 production at both the anode and cathode, augmenting the solar H_2 production rate (Fig. 1b). Consequently, this system represents an efficient approach to harnessing the high photocurrent of c-Si in PEC H_2 production without the need for external bias or a second light absorber.

Highly efficient PtC/Ni/c-Si photocathode

To fabricate a p-n junction-based c-Si photocathode[28,29], we initially prepared an IBC structure c-Si solar cell, wherein all electrodes and doping layers are positioned on the rear side (Fig. 2a). This IBC structure enhances both the J_{SC} and V_{OC} of the c-Si solar cell, which is achieved by minimizing optical loss associated with the front-side electrode in conventional c-Si solar cells and reducing electrical loss attributed to recombination at the front-side doping layer[23,24]. The detailed fabrication process is outlined in the Experimental section and depicted in Supplementary Fig. 1. Subsequently, we encapsulated the c-Si IBC cell using glass and Ni foil to protect it from the electrolyte because c-Si is not stable under alkaline electrolyte conditions. The front side of the c-Si IBC cell was covered with glass (the light-receiving side), while the rear side was connected to the Ni foil (the catalytic reaction side) (Fig. 2a and Supplementary Fig. 2). However, the glass coverage caused a slight optical loss, leading to a reduction in the J_{SC} of the c-Si IBC cell from 39.6 to 37.2 mA cm^{-2} (Fig. 2b and Supplementary Fig. 3). To mitigate the optical loss caused by the glass, we applied an additional MgF_2 antireflection layer, which exhibits negligible absorption (Supplementary Fig. 4), to minimize the refractive index mismatch between the glass and c-Si. Consequently, the difference in J_{SC} between the c-Si IBC cell (39.6 mA cm^{-2}) and the cell with the MgF_2 layer and glass (39.4 mA cm^{-2}) was negligible (Supplementary Fig. 3). Subsequently, we affixed a commercial PtC (platinum on graphitized carbon) catalyst loaded on carbon paper, known for its high activity in the HER, to the Ni foil (referred to as PtC/Ni/c-Si) to facilitate rapid electron transfer to the electrolyte, ensuring efficient production of H_2[30]. Finally, we coated the PtC/Ni/c-Si photocathode with epoxy on the side to protect c-Si in the electrolyte and secure the catalytic reaction site. Under light illumination, photogenerated electrons in the c-Si IBC cell migrate to the connected Ni foil and PtC catalyst, subsequently reducing water to H_2 (Fig. 2a).

The photoelectrocatalytic performance of the resulting PtC/Ni/c-Si photocathode was evaluated in 1 M NaOH under standard one sun (AM 1.5 G) illumination with a three-electrode configuration. It exhibited a saturated photocurrent density of 39.01 mA cm^{-2} and an onset potential of 0.63 V vs. RHE at 1 mA cm^{-2} (Fig. 2c). The onset potential of the PtC/Ni/c-Si photocathode was positively shifted by ~0.65 V compared to that of the PtC electrocatalyst, which was consistent with the V_{OC} of the c-Si IBC cell (Supplementary Fig. 3). The Ni/c-Si photocathode without PtC showed a negative shift of ~0.2 V in the onset potential, illustrating the role of PtC as an HER catalyst (Supplementary Fig. 5). This well-matched photocurrent density and onset potential

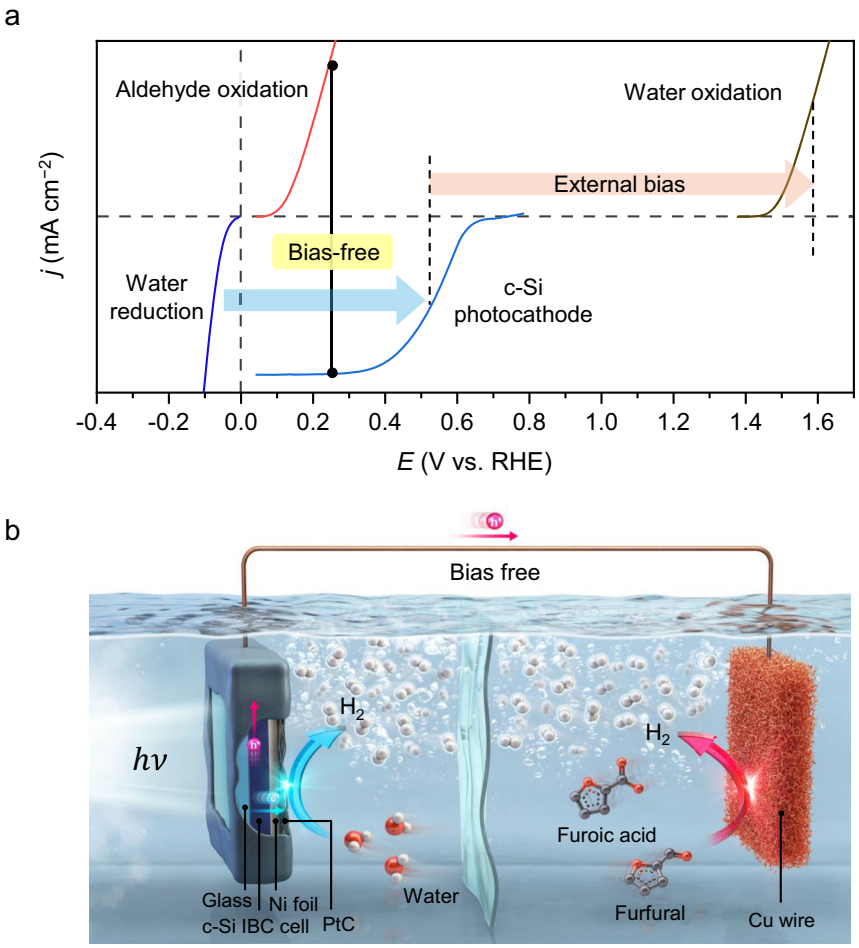

Fig. 1 | Schematic diagram of PEC H_2 production using the PtC/Ni/c-Si photocathode. a LSV curves of aldehyde oxidation, water oxidation, and water reduction. **b** Bias-free PEC dual H_2 production system with the highly efficient PtC/Ni/c-Si photocathode.

indicate the successful fabrication of the PtC/Ni/c-Si photocathode using glass and Ni foil by efficiently protecting the c-Si IBC cell from the alkaline solution. In contrast, the c-Si photocathode without Ni foil encapsulation showed inferior photocurrent density and onset potential due to the instability of the c-Si IBC cell in alkaline electrolyte and the absence of a suitable catalyst (Supplementary Fig. 6). Conclusively, the PtC/Ni/c-Si photocathode demonstrated remarkable stability over 24 h at a constant applied potential of 0.26 V vs. RHE, with negligible changes observed in its LSV curve following chronoamperometry measurements (Fig. 2d and Supplementary Fig. 7). Furthermore, the H_2 production Faradaic efficiency of the PtC/Ni/c-Si photocathode was confirmed to be 100% (Supplementary Fig. 8).

Moreover, we investigated the cooling effect induced by the electrolyte, which impacts the photovoltage of the PtC/Ni/c-Si photocathode. Typically, light-induced temperature elevation activates defect sites in the c-Si, accelerating internal carrier recombination and resulting in a decrease in V_{OC}[31]. To examine this, we captured thermal camera images of the encapsulated c-Si IBC cell (equivalent to the PtC/Ni/c-Si photocathode) in the atmosphere and the PtC/Ni/c-Si photocathode immersed in the electrolyte under continuous solar light exposure. As depicted in Fig. 2e, f, after 180 min, the temperature of the encapsulated c-Si IBC cell in the atmosphere was over 15 °C higher than that of the PtC/Ni/c-Si photocathode in the electrolyte. Additionally, the temperature of the encapsulated c-Si IBC cell in the atmosphere reached saturation faster than the PtC/Ni/c-Si photocathode in the electrolyte (Fig. 2g). Consequently, the V_{OC} of the encapsulated c-Si IBC cell at saturation decreased by over 40 mV (Fig. 2h), whereas the photovoltage of the PtC/Ni/c-Si photocathode in the electrolyte exhibited a comparatively minor decrease of 10 mV (Fig. 2i). This indicates that the cooling effect induced by the electrolyte minimized the photovoltage loss of the c-Si. Despite the efficient fabrication of the PtC/Ni/c-Si photocathode with minimal photovoltage loss, the LSV curves for the HER on the PtC/Ni/c-Si photocathode and the OER on Ni foam do not intersect due to the inherent photovoltage limit of c-Si (Supplementary Fig. 9).

Low-potential furfural oxidation on Cu

As discussed earlier, Wang et al. reported on the low-potential aldehyde oxidation on metallic Cu at a lower onset potential (~0 V vs. RHE) compared with conventional organic oxidation (>1.0 V vs. RHE) and OER (>1.23 V vs. RHE)[22,26,27]. This reaction enables the release of H atoms from the aldehyde as H_2 gas, yielding value-added carboxylic acid as oxidation products of the aldehyde ($R-CHO + 2OH^- \rightarrow R-COO^- + 1/2\ H_2 + H_2O + e^-$). We also fabricated a metallic Cu wire matrix using the same procedure involving chemical oxidation, annealing, and electroreduction of Cu foam to increase surface area[22]. The successful fabrication of metallic Cu wires was confirmed through X-ray diffraction, high-resolution transmission electron microscopy (HRTEM), and scanning electron microscopy (SEM). The X-ray diffraction pattern and HRTEM image indicated that Cu_2O was well converted to metallic Cu through electroreduction (Fig. 3a, b and Supplementary Fig. 10). Additionally, the SEM image revealed the formation of a bent wire structure (Fig. 3c).

The LSV curves of the Cu wire in 1 M NaOH, with and without furfural, confirmed the activity of furfural on Cu, displaying an anodic onset potential (0.0 V vs. RHE) and a distinct oxidation peak of Cu^0 to

https://doi.org/10.1038/s41467-025-58000-4

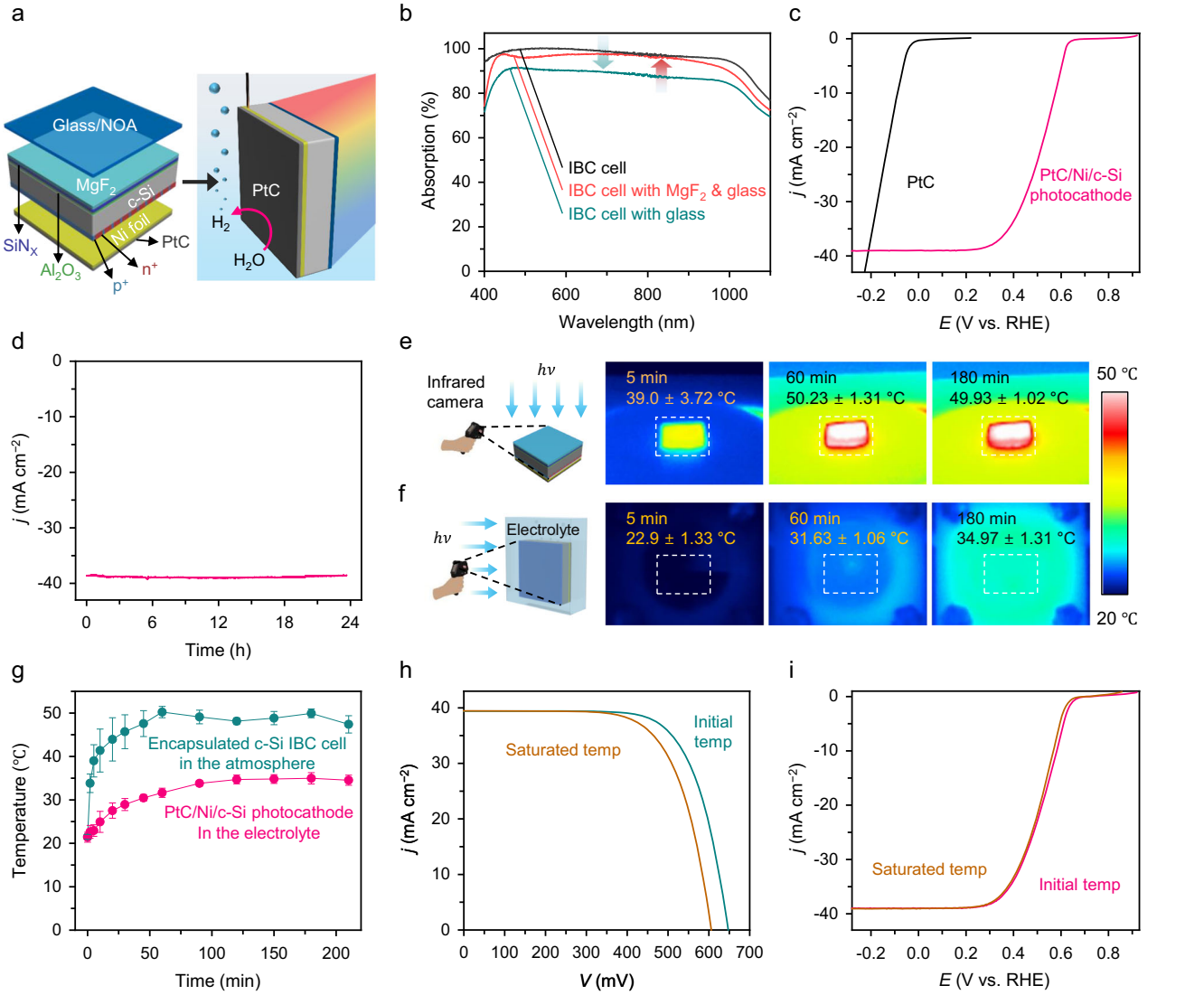

Fig. 2 | Schematic diagram of the PtC/Ni/c-Si photocathode and its performance. a Fabrication scheme of the PtC/Ni/c-Si photocathode. **b** Absorption spectra of the IBC cell depending on the structure. **c** LSV curves of the PtC/Ni/c-Si photocathode. **d** Chronoamperometry measurement of the PtC/Ni/c-Si photocathode at 0.26 V vs. RHE. Changes in the thermal images of the encapsulated c-Si IBC cell in the atmosphere (**e**) and the PtC/Ni/c-Si photocathode in the electrolyte (**f**) under continuous light illumination. **g** Temperature profile of the encapsulated c-Si IBC cell in the atmosphere and the PtC/Ni/c-Si photocathode in the electrolyte. **h** Temperature-dependent current density–voltage curves of the encapsulated c-Si IBC cell. **i** Temperature-dependent LSV curve of the PtC/Ni/c-Si photocathode. All PEC performances were measured under one sun illumination (AM 1.5 G) in 1 M NaOH. The error bars indicate the standard deviation based on three independent measurements. Source data are provided as a Source Data file.

Cu^+ at ~0.5 V vs. RHE (Fig. 3d). This lower onset potential of furfural oxidation compared with that of OER allowed bias-free operation with the PtC/Ni/c-Si photocathode, achieving an intersecting point at 38.61 mA cm^{-2} at 0.26 V vs. RHE (Supplementary Fig. 11). We analyzed the organic products in the electrolyte using high-performance liquid chromatography (Supplementary Fig. 12). During electrolysis on the Cu wire at a constant potential of 0.3 V vs. RHE in 1 M NaOH solution containing furfural, the furfural concentration decreased over time as it was converted to furoic acid by electrooxidation on Cu, accounting for the fast decrease in current density (Fig. 3e, Supplementary Fig. 13 and 14). When the solution was refreshed, the decreased current caused by the reduction in the furfural concentration recovered (Supplementary Fig. 15). We also detected a small amount of furfural alcohol generated by the non-Faradaic Cannizzaro reaction. The carbon balances of all reactant and products were well-matched during the reaction (Fig. 3e). The Faradaic efficiencies (%) of furoic acid, after subtracting those produced from the Cannizzaro reaction, ranged from 95 to 100% near the expected operating potential (Fig. 3f). This confirms that furfural oxidation on the Cu wire can successfully work with the HER on the prepared PtC/Ni/c-Si photocathode. Furthermore, there was no observed electrocatalytic activity of the Cu wire for both products (Supplementary Fig. 16). The gaseous H_2 was also separately analyzed by gas chromatography, and the Faradaic efficiencies of H_2 were also high (95–100%) over the same potential range (Fig. 3f and Supplementary Fig. 17). This suggests the feasibility of achieving a high 1-sun H_2 production rate through dual H_2 production when integrating the Cu wire with the PtC/Ni/c-Si photocathode. Chronoamperometry measurement with continuous furfural supply at a constant applied potential of 0.26 V vs. RHE showed that the anodic current of the Cu wire slightly decreased over 10 h (Supplementary Fig. 18). While no changes were observed in the crystalline structure or morphology after electrolysis (Supplementary Fig. 19), partial oxidation and Cu leaching were noted. The Cu K-edge X-ray absorption near-edge structure (XANES) spectra of the spent Cu wire catalyst displayed a

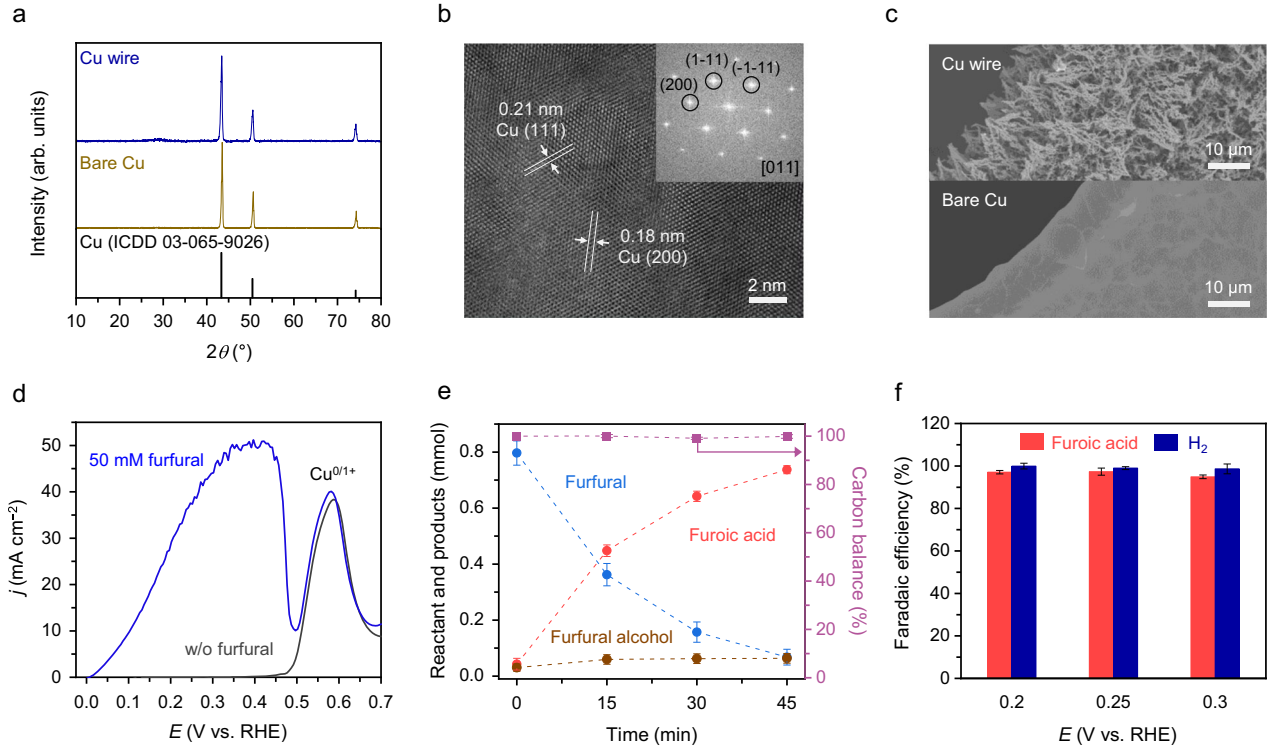

Fig. 3 | Characterization and furfural oxidation activities of the Cu wire catalyst. a X-ray diffraction patterns of Cu wire and bare Cu. **b** HRTEM image of Cu wire. Inset: fast Fourier transform pattern. **c** SEM images of Cu wire and bare Cu. **d** LSV curves of Cu wire in 1 M NaOH with and without 50 mM furfural **e** The amount of reactant and products and carbon balance over time during the electrolysis at 0.3 V vs. RHE. **f** Furoic acid and H_2 Faradaic efficiency of Cu wire at 0.2–0.3 V vs. RHE. All electrocatalytic activities were measured in 1 M NaOH with 50 mM furfural. The error bars indicate the standard deviation based on three independent measurements. Source data are provided as a Source Data file.

slightly lower pre-edge peak intensity ($1s \rightarrow 4p_z$) and a higher white-line peak intensity ($1s \rightarrow 4p_{x,y}$) than the fresh Cu wire catalyst, indicating a higher oxidation state (Supplementary Fig. 20)[32]. Furthermore, the Cu_2O catalyst without electroreduction pretreatment exhibited significantly lower activity than the metallic Cu catalyst, suggesting that Cu^0 species in the Cu wire catalyst serve as the main active sites for the furfural oxidation reaction (Supplementary Fig. 21). Therefore, the partial oxidation of the Cu wire, as observed through XANES, likely contributed to the reduced catalytic activity[33]. In addition, Cu leaching during electrolysis was observed, leading to the loss of active sites (Supplementary Table 1). Consequently, the partial oxidation of Cu^0 species and Cu leaching during the furfural oxidation reaction were the primary factors causing the slight decrease in the anodic current of the Cu wire catalyst.

Bias-free dual H_2 production: fourfold increase over DOE target

Finally, we established a PEC dual H_2 production system utilizing the PtC/Ni/c-Si photocathode and the Cu wire. The PEC reactor comprised two compartments, one each of oxidation and reduction cell, separated by an anion exchange membrane, akin to a conventional water-splitting reactor. To evaluate the bias-free PEC H_2 production of the system, we measured PEC performances in a two-electrode configuration under AM 1.5 G illumination (Fig. 4a). The observed photocurrent density (37.8 mA cm^{-2}) stemming from furfural oxidation and HER at 0 V clearly indicates that the PtC/Ni/c-Si photocathode can produce H_2 without requiring an additional potential, efficiently utilizing the maximum photocurrent of the PtC/Ni/c-Si photocathode. Conversely, conventional water splitting using the PtC/Ni/c-Si photocathode and Ni foam exhibited no photoactivity at 0 V, affirming the unattainability of bias-free operation. Additionally, we compared water splitting using a modularized PtC/Ni/c-Si photocathode, aligning with strategies reported by various groups, including our own, which involve modularization techniques or the use of Si triple-junction for bias-free water splitting[19–21,34]. The modularized PtC/Ni/c-Si photocathode, constructed by interconnecting three c-Si IBC unit cells in series, effectively tripled the total photovoltage but concurrently reduced the current density to one-third of its original photocurrent density due to the increased illumination area (Supplementary Fig. 22). Consequently, the modularized PtC/Ni/c-Si photocathode achieved an intersecting point with Ni foam (Supplementary Fig. 23). However, it fell short of fully harnessing the high inherent photocurrent of c-Si, resulting in a lower operating photocurrent density (9.4 mA cm^{-2}), compared with the dual H_2 production (Fig. 4a).

The actual PEC dual H_2 production was carried out by continuously supplying 50 mM furfural in 1 M NaOH to the oxidation cell, exhibiting a high photocurrent density for over 10 h (Fig. 4b). Although a slight decrease was observed after 4 h due to Cu wire deactivation, the overall performance degradation was less pronounced compared to the stability of Cu wire after integration with the PtC/Ni/c-Si photocathode (Fig. 4b, Supplementary Fig. 18 and 24). The Faradaic efficiency of our system approached 200% during PEC operation, achieving a remarkable solar H_2 production rate of 1.40 mmol h^{-1} cm^{-2} (Fig. 4c). This rate was 8.1 times higher than that of water splitting using the modularized PtC/Ni/c-Si photocathode, attributed not only to a higher operating photocurrent density but also to dual-sided H_2 production. The different H_2 sources at the anode and cathode were confirmed by gas chromatography–mass spectrometry using deuterated benzaldehyde (C_6H_5–CDO) as the oxidative reactant. The mass spectrum of collected H_2 from the anode and cathode cells showed an intense signal at m/z = 4 (D_2) and at m/z = 2 (H_2), respectively, indicating that the proton source for produced H_2 at the anode was the aldehyde group, while at the cathode, it was water (Fig. 4d). In

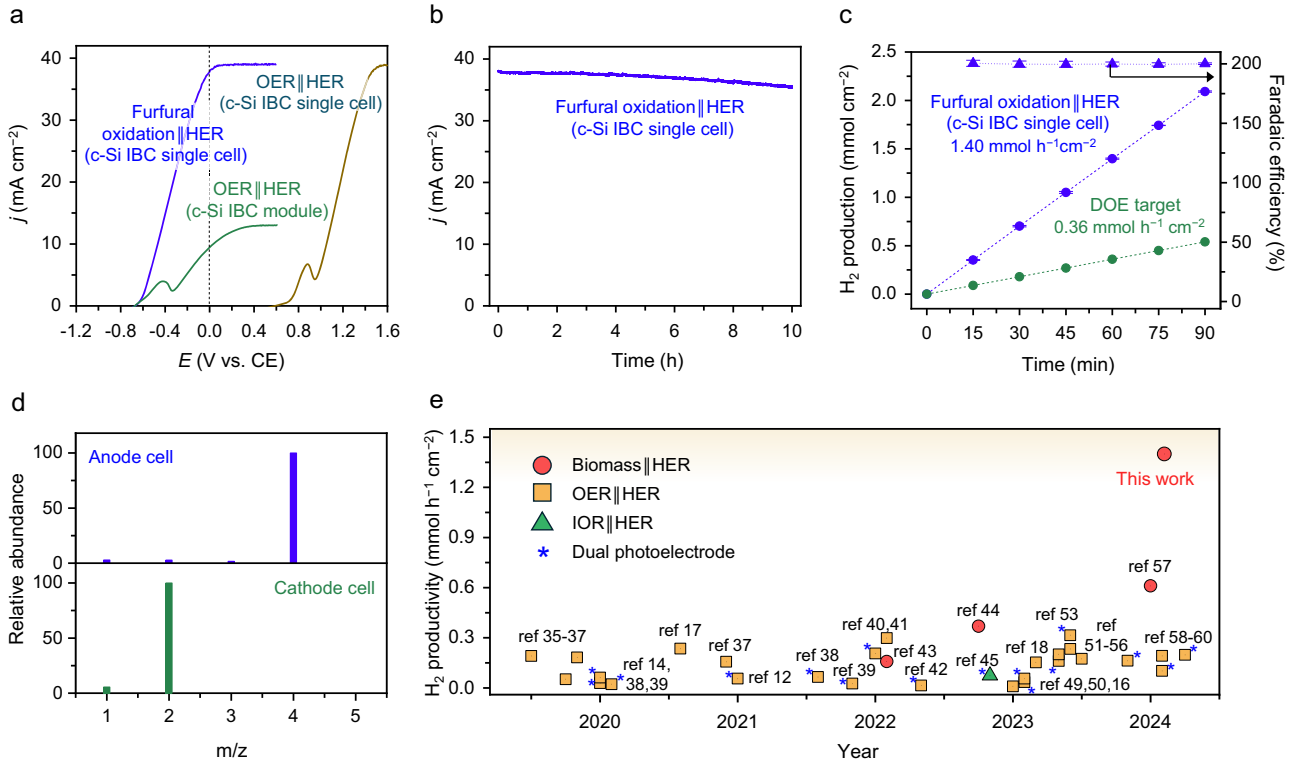

Fig. 4 | Overall bias-free PEC H_2 production. a LSV curves of furfural oxidation with HER, OER with HER using the PtC/Ni/c-Si photocathode, and LSV curves of OER with HER using the modularized PtC/Ni/c-Si photocathode in the two-electrode configuration. **b** Chronoamperometry of dual H_2 production using the PtC/Ni/c-Si photocathode at 0 V. **c** Produced H_2 and its Faradaic efficiency for dual H_2 production. **d** Mass spectra of collected gas from anode and cathode sides during the bias-free C_6H_5–CDO oxidation and HER. **e** H_2 production rate comparison with previously reported bias-free PEC H_2 production system. Biomass: Biomass oxidation reaction, IOR: iodide oxidation reaction, Dual photoelectrode (Photoanode‖Photocathode). The experiments were conducted in 1 M NaOH with (for dual H_2 production) and without 50 mM furfural (for water splitting) in the two-electrode configuration under AM 1.5 G illumination. The error bars indicate the standard deviation based on three independent measurements. Source data are provided as a Source Data file.

conclusion, our 1-sun H_2 production rate (1.40 mmol h^{-1} cm^{-2}) establishes a high record value, far surpassing previously reported bias-free PEC H_2 production (Fig. 4e and Supplementary Table. 2)[14–16,20,21,35–60].

Discussion

Notably, electrolysis using electricity is expected to demand a higher current than PEC H_2 production for practical implementation. However, increasing the current by applying a high potential over 0.5 V vs. RHE is impeded by the electrooxidation of Cu^0 to Cu^+ (Fig. 3d)[61]. Moreover, the cost of electricity must be considered. Nevertheless, the photocurrent density of bias-free PEC H_2 production in our system is ~40 mA cm^{-2}, corresponding to a potential of ~0.3 V vs. RHE where Cu oxidation does not occur easily (Supplementary Fig. 11). Therefore, dual H_2 production using a Cu catalyst is highly suitable in the PEC system. We achieved a 1.40 mmol h^{-1} cm^{-2} 1-sun H_2 production rate, surpassing the DOE target by fourfold. Furthermore, we demonstrated that the partial oxidation and leaching of Cu^0 species during the furfural oxidation reaction led to a slight decrease in the stability of the Cu wire catalyst. Thus, as the stability of the Cu catalyst improves through further studies, such as utilizing redox polymers[62] and doping with secondary metals[63] to mitigate its oxidation and leaching, this accomplishment potentially aligns PEC H_2 production technology with H_2 production from fossil fuels.

To support this advancement, the supply of furfural must be increased. Although the current annual furfural production is lower than that of H_2 production (85 million tons/year)[64], furfural is a prominent biomass-derived platform molecule that can be produced from the most abundant lignocellulosic biomass, which has an estimated annual production of 200,000 million tons[65]. However, scalable furfural production is challenging due to current technical limitations arising from the chemical and structural diversity of lignocellulose[66]. Fortunately, there has been increasing interest in research on utilizing lignocellulosic biomass to produce bio-platform molecules such as furfural and 5-hydroxymethylfurfural (HMF)[66,67]. Furthermore, if the demand for furfural increases, driven by the outcomes of H_2 production, we anticipate further advancements in furfural production technologies. In addition, the furfural oxidation reaction in the proposed system can also be replaced with other aldehydes, following the same mechanism[22,68]. A range of aldehydes, such as formaldehyde (32 million tons/year), acetaldehyde (1–2 million tons/year), and HMF, can be used[69,70]. Therefore, the abundant supply of lignocellulosic biomass for furfural production and the applicability of this technology to other aldehydes indicate that, in the long term, it could satisfy a substantial portion of the H_2 production demand. We believe that this highly efficient system, maximizing the high photocurrent of c-Si, represents a significant advancement toward practical solar-to-H_2 production in real-world applications.

Methods

Materials

Commercial Cu (99.96%) and Ni foam (99.97%) were purchased from MTI, Korea. Isopropanol, hydrochloric acid (1 M), and alkaline solutions (1, 2 M NaOH, and 1 M KOH) were obtained from Samchun Chemical. Ni foil (99.5%, 100 μm thickness), NaOH pellets (98%), methanol (HPLC grade, 99.8%), and 10 mM ammonium formate in water (HPLC grade) were sourced from Alfa Aesar. Furfural (99%), furoic acid (98%),

furfural alcohol (98%), ammonium persulfate (98%), sulfuric acid (98%, HPLC grade), Nafion dispersion (5 wt%), and platinum on graphitized carbon (PtC, 20 wt%) were purchased from Sigma Aldrich. Water (HPLC grade) was obtained from JT Baker. Benzaldehyde-α-d_1 (98 atom % D) was acquired from CDN isotopes Inc. Ag paste (Elcoat P-100) was sourced from CANS. Selemion ion exchange membrane (AMVN) was obtained from AGC Engineering Co. Hydrophilic carbon paper (HCP020N) was purchased from WizMAC. P-type c-Si wafers were procured from Zhejiang Zhongguang Electrical Co. Ltd. Spin-on dopant sources (P509 and B155) were sourced from Filmtronics. Epoxy was obtained from JB Weld. DPR-i 1549 photoresist was sourced from Dongjin Semichem. Ag pellets with 99.99% purity, used as metal electrodes for IBC c-Si solar cells, were sourced from KRT. Transparent ultraviolet-curable polymer (NOA 63) was purchased from Norland Products, Inc.

Fabrication of c-Si IBC solar cells

The c-Si IBC solar cells were fabricated using p-type c-Si wafers with a resistivity of 1–3 Ω cm and a thickness of 120 µm. On the rear side of the c-Si IBC cell, interdigitated emitter and back surface field were formed in selective areas. For selective doping, patterned SiO_2 (900 nm thickness) served as a diffusion barrier. Plasma-enhanced chemical vapor deposition (PE-CVD; PEH-600, Sorona, Anseong-si, South Korea) was utilized to deposit SiO_2, followed by photolithography using DPR-i 1549 photoresist and an etch-back process using buffered oxide etchant (BOE) solution. The back surface field (BSF) layer was formed in a mixed atmosphere of O_2 (250 sccm) and N_2 (1000 sccm) at 1000 °C in a tube furnace, using a boron dopant source. The emitter doping was carried out under the same process conditions. After fabricating the patterned SiO_2, the emitter layer was formed using a phosphorus dopant source at 840 °C in a tube furnace with an O_2 (125 sccm) and N_2 (500 sccm) atmosphere. An Al_2O_3 passivation layer was deposited via atomic layer deposition (Lucida D100, NCD), followed by annealing in a mixed atmosphere of Ar/H_2 (96:4) at 500 °C with a flow rate of 500 sccm. A 60 nm-thick SiNx layer was deposited via PE-CVD as an anti-reflection layer. A photolithography process was carried out using DPR-i 1549 photoresist to develop an interdigitated electrode as the rear electrode. The electrodes were formed by depositing 1 µm-thick Ag films using a thermal evaporator.

Fabrication of c-Si IBC module

The c-Si IBC cells were aligned on the glass substrate for series connection. Each c-Si IBC unit cell was affixed to the glass using NOA 63, while connections between the emitter of one unit cell and the BSF portion of another were established using the Ag paste.

Characterization of c-Si IBC cells and modules

The optical transmittance and reflectance of the c-Si IBC cells were assessed across the wavelength range of 300–1100 nm using a UV–Vis/NIR spectrophotometer (Cary 5000, Agilent) equipped with a 110 mm integrating sphere to capture total light (diffuse and specular) reflection. Current density–voltage characteristics of both c-Si IBC cells and modules were examined using an Oriel Sol3A class AAA solar simulator (Newport) under AM 1.5 G illumination at 25 °C in air. Incident flux was measured using a calibrated power meter and confirmed using a solar cell calibrated by the National Renewable Energy Laboratory, USA (PV Measurements, Inc.). Thermal distribution images of the c-Si IBC cells were captured using an infrared camera (Testo 870, Testo Korea Ltd).

Fabrication of PtC/Ni/c-Si photocathode

The front side of the c-Si IBC cell (1 × 1 cm) was passivated with NOA 63 and glass, while the Cu wire was attached to the p-type region on the rear side using the Ag paste to fabricate the photocathode. NOA 63 is a colorless and transparent optical adhesive used to adhere glass to the c-Si IBC cell (Supplementary Fig. 25). Subsequently, a PtC-attached Ni foil (1 × 1 cm) was connected to the n-type region on the rear side using the Ag paste. Epoxy was applied to cover the entire area, excluding the c-Si IBC cell and the PtC. The PtC-attached Ni foil was prepared as follows: PtC catalyst ink was prepared by mixing 5 mg of PtC powder, 1 mL of ethanol, and 10 µL of Nafion dispersion. This ink was then drop-casted onto a hydrophilic carbon paper (178 µL cm^{-2}), and the PtC-loaded carbon paper (0.88 mg cm^{-2}) was connected to Ni foil using the electroconductive Ag paste. The fabrication scheme and digital photographs of the fabricated PtC/Ni/c-Si photocathode are shown in Supplementary Fig. 2.

Fabrication of Cu wire

Commercial Cu foam (1 × 1 cm) underwent a thorough cleaning process with isopropanol followed by 1 M HCl to cleanse the surface. The cleaned Cu foam was immersed in an aqueous solution containing 2.67 M NaOH and 0.13 M $(NH_4)_2S_2O_8$ for 2 h at 40 °C to facilitate the growth of the $Cu(OH)_2$ wire on the surface. After washing, the synthesized $Cu(OH)_2$ wire was annealed in a flowing Ar atmosphere at 550 °C for 3 h, converting it to Cu_2O. Finally, an electrochemical reduction step was performed in a three-electrode configuration at −100 mA cm^{-2} for 10 min in 1 M KOH to convert Cu_2O to metallic Cu.

Characterization of Cu wire

X-ray diffraction patterns of Cu catalysts were recorded using a D8 ADVANCE diffractometer (Bruker AXS) with Cu Kα radiation (λ = 1.5406 Å) over a diffraction angle (2θ) range of 10–80°, with a step size of 0.02°. SEM and high-resolution HRTEM images were acquired using a SU8220 microscope (Hitachi High-Technologies) and a JEM-2100F microscope (JEOL), respectively. For HRTEM analysis, sample preparation was conducted using a Helios 450HP FIB (FEI). The Cu K-edge XANES spectra (E_0 = 8979 eV) were recorded in the fluorescence mode at the 6D beamline in the Pohang Accelerator Laboratory, Republic of Korea. The incident beam was detuned to 70% of its maximum value using a Si (111) double-crystal monochromator to eliminate higher-order harmonics. For XANES measurements, Cu wire catalysts were ultrasonicated in ethanol and then spray-coated onto the carbon paper substrate. The concentration of Cu in the electrolyte was determined through inductively coupled plasma optical emission spectroscopy (Varian 700-ES).

Electrochemical measurements and product analysis for furfural oxidation

All electrochemical measurements were performed using an Ivium-Stat.h electrochemical workstation (Ivium Technologies). The LSV curve of the Cu catalyst for furfural oxidation was obtained in a three-electrode configuration utilizing a Hg/HgO reference electrode (RE-61AP, ALS Co., Ltd) and a Pt wire counter electrode in 17 mL of 1 M NaOH with 50 mM furfural from −0.1 to 0.7 V vs. RHE at a scan rate of 1.5 mV s^{-1}. *iR* (*i*, current; *R*, resistance)-Compensation was not performed. Chronoamperometry measurements were carried out in a custom-made H-type acryl reactor with 17 mL of anolyte (1 M NaOH with 50 mM furfural) and 35 mL of catholyte (1 M NaOH).

For liquid product analysis, anolyte and catholyte samples were subjected to high-performance liquid chromatography (HPLC, 1260 Infinity, Agilent) using a UV-Vis detector at 220 nm. Each sample was mixed with 0.5 M H_2SO_4 to adjust the pH to 7 and then diluted with deionized water to fall within the calibration curve range. The analysis utilized a Zorbax Eclipse XDB-C18 column (Agilent) with the following parameters: analysis time of 10 min, flow rate of 0.6 mL min^{-1}, and column temperature of 50 °C. The mobile carrier was a 3:7 ratio mixture of methanol and 5 mM ammonium formate solution. The quantification of the reaction was based on a linear external standard curve (R^2 > 0.99) of the respective compound. Carbon balance and Faradaic efficiency of furoic acid (after subtracting furoic acid produced from the Cannizzaro reaction) were calculated according to the following

equations:

$$\text{Carbon balance}\,(\%) = \frac{\text{total amount of reactant and products during the reaction}}{\text{total amount of reactant and product at the beginning}} \times 100 \quad (1)$$

$$\text{Faradaic efficiency of furoic acid}\,(\%) = \frac{(\text{amount of furoic acid} - \text{amount of furfural alcohol}) \times nF}{Q} \times 100 \quad (2)$$

where n, F, and Q indicate the number of transferred electrons (1), Faraday constant, and total charge passed during the reaction, respectively.

Gas product analysis involved continuously bubbling Ar gas (99.999%) into the anode electrolyte, with outlet gas lines connected directly to a gas chromatograph (6500GC system, YL Instrument) equipped with a molecular sieve 13X column (Supelco) and thermal conductivity detector. The Faradaic efficiency of H_2 was calculated as follows:

$$\text{Faradaic efficiency of } H_2\,(\%) = \frac{\text{detected amount of } H_2 \times nF}{Q} \times 100 \quad (3)$$

where n, F, and Q indicate the number of transferred electrons (2), Faraday constant, and total charge passed during the reaction, respectively.

PEC measurements

All PEC measurements were conducted using the same electrochemical workstation. The performance of the c-Si photocathode (1 cm^2) was assessed in a three-electrode configuration from 1.0 to −0.4 V vs. RHE in 1 M NaOH, with illumination from an Oriel Sol3A class AAA solar simulator (Newport) directed onto the glass side. The light intensity at the sample position was adjusted to 100 mW cm^{-2} (AM 1.5 G) using a reference Si cell (91,150 V, Newport).

Bias-free PEC H_2 production

The overall H_2 production was conducted in an H-type acrylic reactor comprising an anode cell and a cathode cell, each equipped with a quartz window. The anode and cathode cells contained 17 mL of 1 M NaOH with 50 mM furfural and 35 mL of 1 M NaOH, respectively. Separation between the anode and cathode cells was achieved using a Selemion anion exchange membrane. To facilitate dual H_2 production involving furfural oxidation and the HER simultaneously, a two-electrode configuration was employed, with a Cu wire catalyst as the working electrode and the c-Si photocathode as the counter electrode. For continuous furfural supply, fresh electrolyte was delivered to the anodic cell at a total flow rate of 1.4 mL min^{-1} (0.7 mL min^{-1} of 100 mM furfural and 0.7 mL min^{-1} of 2 M NaOH) using a peristaltic pump (JWTE 600, JenieWell). Ar gas (99.999%) was continuously purged into both cells to detect H_2 gas, and the outlet gas lines were directly connected to a gas chromatograph (6500GC system, YL Instrument). Mass spectra of collected gases from benzaldehyde-α-d_1 oxidation and HER were recorded using a quadrupole mass spectrometer (QMG 220, Pfeiffer).

For PEC water splitting involving the OER and HER, commercial Ni foam was utilized as the working electrode for the OER catalyst, while the c-Si photocathode functioned as the counter electrode for HER.

Data availability

The data generated in this study have been deposited in the Figshare repository (https://doi.org/10.6084/m9.figshare.28477688)[71]. Source data are provided with this paper.

References

1. Lewis, N. S. Research opportunities to advance solar energy utilization. *Science* **351**, aad1920 (2016).
2. Walter, M. G. et al. Solar water splitting cells. *Chem. Rev.* **110**, 6446–6473 (2010).
3. Gao, R.-T. et al. Single-atomic-site platinum steers photogenerated charge carrier lifetime of hematite nanoflakes for photoelectrochemical water splitting. *Nat. Commun.* **14**, 2640 (2023).
4. Gao, R.-T. et al. Dynamic semiconductor-electrolyte interface for sustainable solar water splitting over 600 h under neutral conditions. *Sci. Adv.* **9**, eade4589 (2023).
5. Gao, R.-T. et al. Ru-P pair sites boost charge transport in hematite photoanodes for exceeding 1% efficient solar water splitting. *Proc. Natl. Acad. Sci. USA.* **120**, e2300493120 (2023).
6. Pal, A. et al. Powering squarely into the future: a strategic analysis of hydrogen energy in QUAD nations. *Int. J. Hydrog. Energy* **49**, 16–41 (2024).
7. Safari, F. & Dincer, I. A review and comparative evaluation of thermochemical water splitting cycles for hydrogen production. *Energy Convers. Manag.* **205**, 112182 (2020).
8. Kim, N., Choi, D., Kim, H., Um, H.-D. & Seo, K. Silicon microwire arrays with nanoscale spacing for radial junction c-si solar cells with an efficiency of 20.5. *ACS Nano* **15**, 14756–14765 (2021).
9. Fan, R., Mi, Z. & Shen, M. Silicon based photoelectrodes for photoelectrochemical water splitting. *Opt. Express* **27**, A51–A80 (2019).
10. Luo, Z., Wang, T. & Gong, J. Single-crystal silicon-based electrodes for unbiased solar water splitting: current status and prospects. *Chem. Soc. Rev.* **48**, 2158–2181 (2019).
11. Shih, A. J. et al. Water electrolysis. *Nat. Rev. Methods Prim.* **2**, 84 (2022).
12. Zhou, X. et al. 570 mV photovoltage, stabilized n-Si/CoO_x eterojunction photoanodes fabricated using atomic layer deposition. *Energy Environ. Sci.* **9**, 892–897 (2016).
13. Wu, B. et al. Stable solar water splitting with wettable organic-layer-protected silicon photocathodes. *Nat. Commun.* **13**, 4460 (2022).
14. Liu, B. et al. Bifacial passivation of n-silicon metal–insulator–semiconductor photoelectrodes for efficient oxygen and hydrogen evolution reactions. *Energy Environ. Sci.* **13**, 221–228 (2020).
15. Liu, B. et al. Double-side Si photoelectrode enabled by chemical passivation for photoelectrochemical hydrogen and oxygen evolution reactions. *Adv. Funct. Mater.* **31**, 2007222 (2021).
16. Moon, C. et al. Dual-purpose tunnel oxide passivated contact on silicon photoelectrodes with high photovoltages for tandem photoelectrochemical devices enabling unassisted water splitting. *J. Mater. Chem. A* **11**, 4194–4204 (2023).
17. Shaner, M. R., McDowell, M. T., Pien, A., Atwater, H. A. & Lewis, N. S. Si/TiO_2 tandem-junction microwire arrays for unassisted solar-driven water splitting. *J. Electrochem. Soc.* **163**, H261 (2016).
18. Reece, S. Y. et al. Wireless solar water splitting using silicon-based semiconductors and earth-abundant catalysts. *Science* **334**, 645–648 (2011).
19. Urbain, F. et al. Multijunction Si photocathodes with tunable photovoltages from 2.0 V to 2.8 V for light induced water splitting. *Energy Environ. Sci.* **9**, 145–154 (2016).
20. Fu, H.-C., Varadhan, P., Lin, C.-H. & He, J.-H. Spontaneous solar water splitting with decoupling of light absorption and electrocatalysis using silicon back-buried junction. *Nat. Commun.* **11**, 3930 (2020).
21. Jin, W. et al. Natural leaf-inspired solar water splitting system. *Appl. Catal. B* **322**, 122086 (2023).

22. Wang, T. et al. Combined anodic and cathodic hydrogen production from aldehyde oxidation and hydrogen evolution reaction. *Nat. Catal.* **5**, 66–73 (2022).
23. Richter, A. et al. Design rules for high-efficiency both-sides-contacted silicon solar cells with balanced charge carrier transport and recombination losses. *Nat. Energy* **6**, 429–438 (2021).
24. Richter, A., Glunz, S. W., Werner, F., Schmidt, J. & Cuevas, A. Improved quantitative description of Auger recombination in crystalline silicon. *Phys. Rev. B* **86**, 165202 (2012).
25. Liu, H. et al. Ultra-low voltage bipolar hydrogen production from biomass-derived aldehydes and water in membrane-less electrolyzers. *Energy Environ. Sci.* **15**, 4175–4189 (2022).
26. Wang, T. et al. Transforming electrocatalytic biomass upgrading and hydrogen production from electricity input to electricity output. *Angew. Chem. Int. Ed.* **61**, e202115636 (2022).
27. Na, J. et al. General technoeconomic analysis for electrochemical coproduction coupling carbon dioxide reduction with organic oxidation. *Nat. Commun.* **10**, 5193 (2019).
28. Cox, C. R., Winkler, M. T., Pijpers, J. J. H., Buonassisi, T. & Nocera, D. G. Interfaces between water splitting catalysts and buried silicon junctions. *Energy Environ. Sci.* **6**, 532–538 (2013).
29. Li, Z. et al. Solar hydrogen. *Adv. Energy Mater.* **13**, 2203019 (2023).
30. Li, Y. et al. Implanting Ni-O-VO_X sites into Cu-doped Ni for low-overpotential alkaline hydrogen evolution. *Nat. Commun.* **11**, 2720 (2020).
31. Dubey, S., Sarvaiya, J. N. & Seshadri, B. Temperature dependent photovoltaic (PV) efficiency and its effect on PV production in the world – a review. *Energy Procedia* **33**, 311–321 (2013).
32. Li, S. et al. Reconstruction-induced NiCu-based catalysts toward paired electrochemical refining. *Energy Environ. Sci.* **15**, 3004–3014 (2022).
33. Yang, M. et al. Correlating the valence state with the adsorption behavior of a Cu-based electrocatalyst for furfural oxidation with anodic hydrogen production reaction. *Adv. Mater.* **35**, 2304203 (2023).
34. Trompoukis, C. et al. Porous multi-junction thin-film silicon solar cells for scalable solar water splitting. *Sol. Energy Mater. Sol. Cells* **182**, 196–203 (2018).
35. Wang, Y., Schwartz, J., Gim, J., Hovden, R. & Mi, Z. Stable unassisted solar water splitting on semiconductor photocathodes protected by multifunctional gan nanostructures. *ACS Energy Lett.* **4**, 1541–1548 (2019).
36. Wang, Y. et al. A single-junction cathodic approach for stable unassisted solar water splitting. *Joule* **3**, 2444–2456 (2019).
37. Varadhan, P., Fu, H.-C., Kao, Y.-C., Horng, R.-H. & He, J.-H. An efficient and stable photoelectrochemical system with 9% solar-to-hydrogen conversion efficiency via InGaP/GaAs double junction. *Nat. Commun.* **10**, 5282 (2019).
38. Li, H. et al. Construction of uniform buried pn junctions on pyramid Si photocathodes using a facile and safe spin-on method for photoelectrochemical water splitting. *J. Mater. Chem. A* **8**, 224–230 (2020).
39. Yang, W. et al. Benchmark performance of low-cost Sb_2Se_3 photocathodes for unassisted solar overall water splitting. *Nat. Commun.* **11**, 861 (2020).
40. Vanka, S. et al. InGaN/Si double-junction photocathode for unassisted solar water splitting. *ACS Energy Lett.* **5**, 3741–3751 (2020).
41. Ye, S. et al. Unassisted photoelectrochemical cell with multimediator modulation for solar water splitting exceeding 4% solar-to-hydrogen efficiency. *J. Am. Chem. Soc.* **143**, 12499–12508 (2021).
42. Lee, H. et al. Crystal facet-controlled efficient SNS photocathodes for high performance bias-free solar water splitting. *Adv. Sci.* **8**, 2102458 (2021).
43. Butson, J. D. et al. Surface-structured cocatalyst foils unraveling a pathway to high-performance solar water splitting. *Adv. Energy Mater.* **12**, 2102752 (2022).
44. Wang, M. et al. Integrated and unassisted solar water-splitting system by monolithic perovskite/silicon tandem solar cell. *Sol. RRL* **6**, 2100748 (2022).
45. Hwang, S. W. et al. Sharp-edged nanoflakes array of CuO with enhanced optical and charge transport properties for bias-free tandem solar water-splitting. *Appl. Surf. Sci.* **585**, 152632 (2022).
46. Bhattacharjee, S. et al. Reforming of soluble biomass and plastic derived waste using a bias-free Cu30Pd70|perovskite|Pt photoelectrochemical device. *Adv. Funct. Mater.* **32**, 2109313 (2022).
47. Choi, Y. et al. Bias-free solar hydrogen production at 19.8 mA cm^{-2} using perovskite photocathode and lignocellulosic biomass. *Nat. Commun.* **13**, 5709 (2022).
48. Park, Y. S. et al. High-performance Sb_2S_3 photoanode enabling iodide oxidation reaction for unbiased photoelectrochemical solar fuel production. *Energy Environ. Sci.* **15**, 4725–4737 (2022).
49. Wang, S. et al. An integrated n-Si/$BiVO_4$ photoelectrode with an interfacial bi-layer for unassisted solar water splitting. *Chem. Sci.* **14**, 2192–2199 (2023).
50. Moon, S. et al. Bi_2S_3-Cu_3BiS_3 mixed phase interlayer for high-performance Cu_3BiS_3-photocathode for 2.33% unassisted solar water splitting efficiency. *Adv. Sci.* **10**, 2206286 (2023).
51. Rhee, R. et al. Unassisted overall water splitting with a solar-to-hydrogen efficiency of over 10% by coupled lead halide perovskite photoelectrodes. *Carbon Energy* **5**, e232 (2023).
52. Meng, X. et al. Enabling unassisted solar water splitting with concurrent high efficiency and stability by robust earth-abundant bifunctional electrocatalysts. *Nano Energy* **109**, 108296 (2023).
53. Fehr, A. M. K. et al. Integrated halide perovskite photoelectrochemical cells with solar-driven water-splitting efficiency of 20.8. *Nat. Commun.* **14**, 3797 (2023).
54. Song, Z. et al. All-perovskite tandem photoelectrodes for unassisted solar hydrogen production. *ACS Energy Lett.* **8**, 2611–2619 (2023).
55. Park, J. et al. Hybrid perovskite-based wireless integrated device exceeding a solar to hydrogen conversion efficiency of 11. *Small* **19**, 2300174 (2023).
56. Choi, H. et al. Organometal halide perovskite-based photoelectrochemical module systems for scalable unassisted solar water splitting. *Adv. Sci.* **10**, 2303106 (2023).
57. Mubarok, M. A. et al. Efficient and stable tin–lead perovskite photoconversion devices using dual-functional cathode interlayer. *Adv. Energy Mater.* **14**, 2302555 (2024).
58. Yang, J. W. et al. High-efficiency unbiased water splitting with photoanodes harnessing polycarbazole hole transport layers. *Energy Environ. Sci.* **17**, 2541–2553 (2024).
59. Hwang, S. et al. TiO_2/TiN interface enables integration of Ni_5P_4 electrocatalyst with a III–V tandem photoabsorber for stable unassisted solar-driven water splitting. *ACS Energy Lett.* **9**, 789–797 (2024).
60. Jeong, W. et al. Large-area all-perovskite-based coplanar photoelectrodes for scaled-up solar hydrogen production. *Energy Environ. Sci.* **17**, 3604–3617 (2024).
61. Xiao, L. et al. Coupling electrocatalytic cathodic nitrate reduction with anodic formaldehyde oxidation at ultra-low potential over Cu_2O. *Energy Environ. Sci.* **16**, 2696–2704 (2023).
62. He, W. et al. Enhanced nitrate-to-ammonia efficiency over linear assemblies of copper-cobalt nanophases stabilized by redox polymers. *Adv. Mater.* **35**, 2303050 (2023).
63. Yang, M. et al. A self-reactivated PdCu catalyst for aldehyde electrooxidation with anodic hydrogen production. *Nat. Commun.* **15**, 9852 (2024).

64. Osman, A. I. et al. Hydrogen production, storage, utilisation and environmental impacts: a review. *Environ. Chem. Lett.* **20**, 153–188 (2022).
65. Wang, T., Nolte, M. W. & Shanks, B. H. Catalytic dehydration of C_6 carbohydrates for the production of hydroxymethylfurfural (HMF) as a versatile platform chemical. *Green. Chem.* **16**, 548–572 (2014).
66. Jaswal, A., Singh, P. P. & Mondal, T. Furfural – a versatile, biomass-derived platform chemical for the production of renewable chemicals. *Green. Chem.* **24**, 510–551 (2022).
67. Jing, Y., Guo, Y., Xia, Q., Liu, X. & Wang, Y. Catalytic production of value-added chemicals and liquid fuels from lignocellulosic biomass. *Chem* **5**, 2520–2546 (2019).
68. Li, G. et al. Dual hydrogen production from electrocatalytic water reduction coupled with formaldehyde oxidation via a copper-silver electrocatalyst. *Nat. Commun.* **14**, 525 (2023).
69. Mondal, I., Groves, M., Driver, E. M., Vittori, W. & Halden, R. U. Carcinogenic formaldehyde in US Residential buildings: mass inventories, human health impacts, and associated healthcare costs. *Sci. Total Environ.* **944**, 173640 (2024).
70. Salthammer, T. Acetaldehyde in the indoor environment. *Environ. Sci. Atmos.* **3**, 474–493 (2023).
71. Ko, M. et al. Source data for coupling furfural oxidation for bias-free hydrogen production using crystalline silicon photoelectrodes. figshare https://doi.org/10.6084/m9.figshare.28477688 (2025).

Acknowledgements

We thank UNIST Central Research Facilities (UCRF) for the support of its facilities and equipment. This work was supported by the Korea Institute of Energy Technology Evaluation and Planning (KETEP) and the Ministry of Trade, Industry & Energy (MOTIE) of the Republic of Korea (RS-2024-00488176) through funding to K.S. and J.-W.J. The National Research Foundation (NRF; 2022H1D3A3A01081140, RS-2024-00456139 and RS-2023-00222006) sponsored this study through funding to J.-W.J. This work was also supported by the New Renewable Energy Core Technology Development Project of KETEP granted financial resources from MOTIE (No. 20223030010240) through funding to K.S. In addition, this work was supported by NRF grant funded by the Korean Government (MSIP) (RS-2023-00281706) and MOTIE (RS-2024-00432416) through funding to S.C. and the Ministry of Education (RS-2023-00248296) through funding to M. K.

Author contributions

M.K. and M.L. proposed and designed the experiments under the supervision of J.-W.J., K.S., and S.C. W.Ji. and M.L. fabricated solar cells, solar modules, and photocathodes and measured their performances. M.K., T.K., and W.Ja. synthesized and characterized the Cu wire catalyst with assistance from S.W.H. M.K. and T.K. measured the performance of photocathodes and H_2 productivity. M.K. measured isotopes of H_2 gas using gas chromatography–mass spectrometry with assistance from H.K. and J.H.K. M.K., M.L., T.K., W.Ji., W.Ja., S.C., K.S., and J.-W.J. co-wrote the manuscript. All authors contributed to the discussion and interpretation of the results.

Competing interests

The authors declare no competing interests.

Additional information

Supplementary information The online version contains supplementary material available at https://doi.org/10.1038/s41467-025-58000-4.

Correspondence and requests for materials should be addressed to Seungho Cho, Kwanyong Seo or Ji-Wook Jang.

Peer review information *Nature Communications* thanks Jingying Shi, Rui-Ting Gao, Anna Hankin, and the other anonymous reviewer for their contribution to the peer review of this work. A peer review file is available.